ACS APPLIED MATERIALS & INTERFACES

www.acsami.org

Research Article

Surface Argon Plasma Treatment Enabled Broadband Optoelectronic Synapses Based on Large-Scale Epitaxial GaSe/GaN Heterojunctions

Yunan Lin, Xuecen Miao, Yinuo Zhang, Lan Li, Jiaqi Yang, Hong Lei,* and Yi Pan*

Cite This: *ACS Appl. Mater. Interfaces* 2025, 17, 14257−14268

Read Online

ACCESS | Metrics & More | Article Recommendations | Supporting Information

ABSTRACT: Creating and tuning charge trapping states by introducing atomic-scale defects are crucial for the optoelectronic synapses that parallelize sensing, processing, and memorizing of optical signals in a single device, which is essential for bioinspired neuromorphic computing. Herein, a mild Ar-plasma treatment approach to enable synaptic behavior in 2D semiconductor devices has been proposed and demonstrated in large-scale epitaxial GaSe/GaN heterostructures. The GaSe films were epitaxially grown on a GaN substrate by physical vapor deposition in an ultrahigh vacuum environment, while the devices were fabricated in situ using a shadow mask-assisted electrode deposition technique. A tailored mild Ar-plasma treatment on the GaSe films has been employed to create atomic-scale defects, which provide charge trapping states in the band gap without making morphological damage, as confirmed by the Raman spectra, scanning electron microscopy, and photoluminescence characterizations. Optoelectronic transport measurement under pulsed illumination of varying wavelengths reveals broadband photoresponse and significantly prolonged response time ($\times 10^3$) that give rise to the superior performance of the synaptic devices. This has been proven by the simulation of classic synaptic behaviors of adaptive pain perception and associative learning. Our work provides an efficient approach to facilitate optoelectronic synaptic behaviors in 2D semiconductor devices.

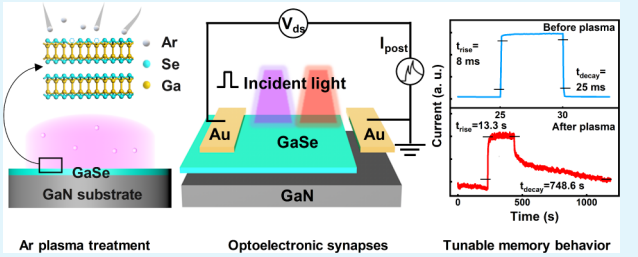

KEYWORDS: *argon plasma treatment, optoelectronic synapses, GaSe/GaN heterojunction, decay time, defect engineering*

1. INTRODUCTION

As the crown jewel of the human body, the brain is considered the seat of intelligence. Thus, neuroscience could provide essential inspiration for artificial intelligence, especially in the renovation of fundamental devices.[1−4] The human brain can store and process data simultaneously with relatively low power consumption and high efficiency, while traditional computers based on von Neumann architecture suffer from low efficiency due to the limited data exchange speed caused by the physical separation of memory and processing modules.[1,3,5,6] This is gradually becoming a serious problem with the increasing computational demands in the big data era. In the human brain, the computation, processing, and transmission of information mainly depend on the interaction of neurons via synapses, which are asymmetric intercellular junctions and communication nodes that mediate rapid point-to-point communication between neurons.[2,7,8] The human brain contains about 10^{11} neurons and 10^{15} synapses, forming a large neuronal circuit that enables the elementary signal processing and memory.[9,10] Thus, mimicking the structure and function of neuronal circuits provides crucial insights for the development of neuromorphic computing. To this end, optoelectronic synaptic devices capable of integrating visual signal perception, information processing, and data storage are highly demanded.

In recent years, artificial optoelectronic synaptic devices have attracted considerable research attention owing to their fascinating advantages and potential applications.[7,11] The optical signal stimulus could provide contactless data input, with the intrinsic advantages of wide bandwidth, strong anti-interference, low resistor−capacitor (RC) delay, and low power consumption. The essential synaptic functions, e.g., short-term plasticity, long-term plasticity, spike-rate-dependent plasticity (SRDP), and spike-timing-dependent plasticity (STDP), have been realized in various optoelectronic materials.[12−19] Among them, the van der Waals (vdW) layered materials are especially promising due to their high optical sensitivity and flexibility.[3,18,20] The memory function of these devices is mainly based on the trapping effect on the

Received: December 20, 2024
Revised: February 17, 2025
Accepted: February 18, 2025
Published: February 24, 2025

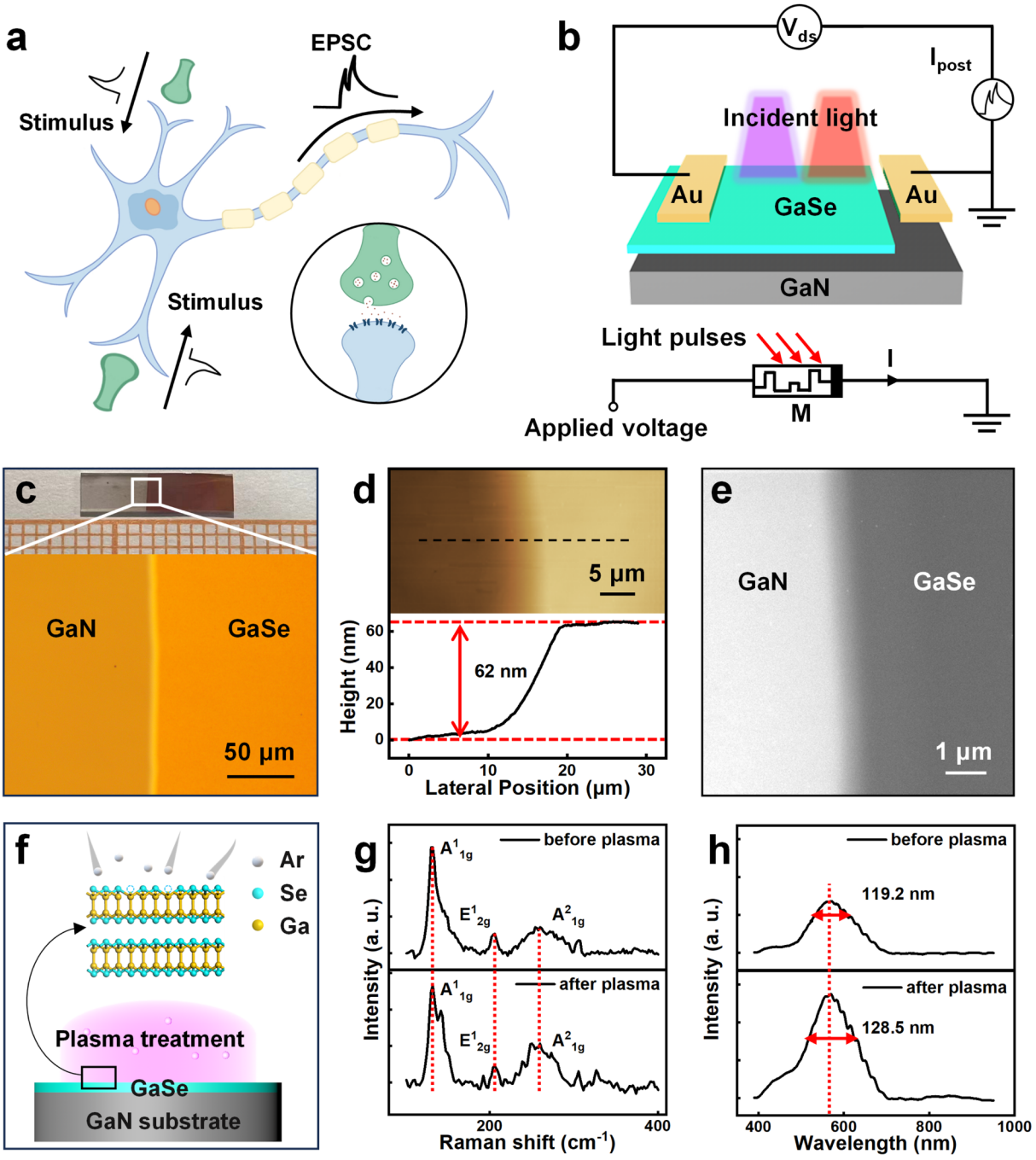

Figure 1. (a) Schematic illustration of neuromorphic signal transmission between biological synapses through the synaptic cleft, which is enlarged in the ring. The memory and processing of the input signals occur spontaneously, generating the EPSC output signal. (b) Upper panel: structure of the artificial optoelectronic synapse based on the two-terminal device of GaSe/GaN heterojunction mimicking the synaptic cleft. Lower panel: simplified circuit diagram showing the functioning mechanism of the device. (c) Upper panel: picture of the GaSe film grown on the right half of GaN substrate. Lower panel: the rectangular enclosed area with the edge of the GaSe film in the OM image. (d) AFM image and the height profile of GaSe film edge. (e) SEM image of the GaSe film after MArP treatment. (f) Schematic illustration demonstrating the MArP treatment that creates atomic scale defects. (g) The Raman and (h) PL spectra obtained from the pristine and Ar-plasma-treated GaSe samples, respectively.

photoexcited carriers.[21] These trapping states mainly originate from the deep levels in the midgap energy of the band. They could prolong the lifetime of photoexcited carriers, enhance the photoconductive gain,[22] and eventually give rise to synaptic behavior. These midgap trapping states originate from the atomic-scale lattice defects such as single vacancies and dopants. Thus, defect engineering has become a powerful tool to promote optoelectronic synaptic behavior in optoelectronic materials.

So far, defect modification methods like high-temperature annealing,[23] oxygen plasma treatment,[24] and electron-beam irradiation[25] have been used to introduce trapping states or optimize the performance of optoelectronic devices. In particular, the surface plasma treatment has shown great potential due to its high efficiency, strength controllability, and compatibility with current semiconductor technology. It has been applied in tuning the fundamental electronic[26] and optical properties[27] of the materials. Nonetheless, the challenge

https://doi.org/10.1021/acsami.4c22477
ACS Appl. Mater. Interfaces 2025, 17, 14257−14268

of the oxygen plasma-assisted defect modification for the vdW layered materials still remains, i.e., the undesirable structural damage and contamination (oxidation) damages due to their nanoscale thickness.[28] Therefore, it is desirable to improve the plasma treatment method for 2D materials sensitive to ion bombardment. A highly controllable plasma treatment for enabling and improving the optoelectronic synaptic behavior in 2D materials, i.e., accomplishing atomic-scale structural modification while minimizing unwanted structural damage and contamination, has yet to be investigated.

In this work, we report a broadband optoelectronic device based on a large-scale epitaxial GaSe/GaN heterojunction with surface argon plasma treatment-enabled robust synaptic functions. The 2D GaSe films were epitaxially grown on n-type GaN substrates by physical vapor deposition in an ultrahigh vacuum (UHV) environment. Subsequently, the devices were fabricated in situ using a shadow mask-assisted electrode deposition technique. Mild Ar-plasma (MArP) treatment was employed to create atomic-scale structural defects that provided deep trap states in the band gap. Photoluminescence (PL) spectroscopy showed that the MArP treatment had made a significant change to the band structure of the sample, revealing the defect-induced energy levels. In the meantime, the phase and morphology of the GaSe films remained intact, as confirmed by Raman spectroscopy and scanning electron microscopy (SEM). Optoelectronic transport measurements demonstrated that the photoresponse time had been prolonged in 10^3 from microsecond (ms) to second (s) levels, confirming the charge trapping effect of the MArP treatment-induced midgap states, which facilitated optical-modulated synaptic functions in the GaSe/GaN heterojunction with enhanced photosensitivity. Benchmark synaptic plasticity indexes like paired-pulse facilitation (PPF) and typical synaptic behaviors, including excitatory postsynaptic current (EPSC), spike-intensity-dependent plasticity (SIDP), spike-number-dependent plasticity (SNDP), and spike-rate-dependent plasticity (SRDP), have been systematically measured with pulsed illumination in varying wavelengths. Based on the broadband photoresponse of the devices, the classic synaptic applications like adapting pain perception and associative learning (Pavlov's dog) were successfully demonstrated. These results suggest that the MArP treatment is a highly efficient universal approach to enable optoelectronic synaptic behaviors in vdW 2D materials, which would find wide application in the production of artificial optoelectronic synapses.

2. RESULTS AND DISCUSSION

2.1. GaSe/GaN Heterojunction with Mild Ar-Plasma Treatment. As shown in Figure 1a, the biological stimuli signals are transmitted from the presynaptic neurons to the postsynaptic neurons through the synaptic cleft as action potential pulses. Specifically, when the action potential of the presynaptic neuron reaches the synaptic terminal, excitatory neurotransmitters in synaptic vesicles are released into the synaptic cleft and further bind to their receptors on the membrane of postsynaptic neurons. The corresponding receptor channels then open up and allow positive ions like sodium (Na^+) and calcium (Ca^{2+}) to flow into postsynaptic neurons, resulting in depolarization of the membrane potential, which forms EPSC and facilitates the transmission of nerve signals and the formation of learning and memory.[29,30] Inspired by the structure of the synaptic cleft, a two-terminal device based on a GaSe/GaN heterojunction, as displayed in Figure 1b, has been designed as an artificial optoelectronic synapse for the perception of the optical stimulus. To achieve efficient optical sensing, high responsivity and broadband photoresponse are required to receive the optical stimuli of various wavelengths. Therefore, GaSe and GaN are selected as photosensitive materials for infrared (IR)−visible (VS) and ultraviolet (UV) lights, respectively. The intrinsic p-type GaSe films are grown on an n-type GaN substrate by utilizing the physical vapor deposition method in a home-built molecular beam epitaxial system with a base pressure of 1×10^{-9} mbar, as shown in Figure S1a. By this way, centimeter-scale high-quality samples with ultraclean interfaces and surfaces are prepared, as displayed in the picture and optical microscope (OM) image in Figure 1c. The AFM height profile is obtained from the topographic image around the edge, as plotted in Figure 1d, which reveals that the GaSe film thickness is about 60 nm. Further AFM measurements given in Figure S1b show the surface roughness of the film is below 1 nm (~0.30 nm) in the whole scanning area of several micrometers, confirming the high homogeneity of the samples.

On the other hand, an appropriate photoresponse time is essential for the memory and signal processing functions. It requires enough defect-induced charge trapping centers in the GaSe film. Since the density of defects in the pristine sample is very low, plasma treatment can be applied to create Se vacancies in the GaSe film. Oxygen plasma treatment is often used to introduce defects and disorders because of its easy availability and high efficacy. However, our test experiments confirmed that the oxygen plasma was unsuitable for GaSe because of unavoidable etching and oxidation, which led to structural damage and transport property degradation. Therefore, we developed a tailored mild Ar-plasma treatment strategy that could not only introduce an appropriate density of defects to enable the synaptic behaviors in the GaSe films but also avoid unwanted damage and contamination. It has been reported previously that the Ar-plasma treatment on MoS_2 is very effective in inducing sulfur vacancies that provide gap states around the Fermi level.[31] Our Ar-plasma intensity has been carefully optimized to a controllable mild level by fine-tuning the Ar pressure to less than 10 Pa while maintaining the flow rate of Ar at about 15 sccm. The plasma treatment time has been optimized as well by evaluating its positive and negative influences on the structure and electronic properties.

To evaluate the effect of the MArP treatment, control experiments were conducted on the same sample before and after that procedure. The SEM image (see Figure 1e) and AFM images (see Figure S1c) taken on the treated sample show that there is no noticeable morphology change, which reveals the defects induced by Ar-plasma are at the atomic scale, as schematically demonstrated in Figure 1f, and the energy dispersive spectrometer (EDS) mappings in Figure S1d−h further prove that the film is little oxidized after plasma treatment. High-resolution transmission electron microscope (TEM) characterization has been utilized on the interface (Figure S1i) to conduct a more in-depth analysis of the defects induced by plasma treatment, which confirmed that the defects created by Ar plasma treatment are mainly vacancies (Figure S2). They decrease from the surface to the inner part of the film with a penetration depth of about a few dozen nanometers. In Figure 1g upper panel, the Raman spectrum obtained from the pristine sample shows distinct peaks located at 130.2 cm^{-1}, 205.9 cm^{-1}, and 255.8 cm^{-1}, corresponding to

https://doi.org/10.1021/acsami.4c22477
ACS Appl. Mater. Interfaces 2025, 17, 14257−14268

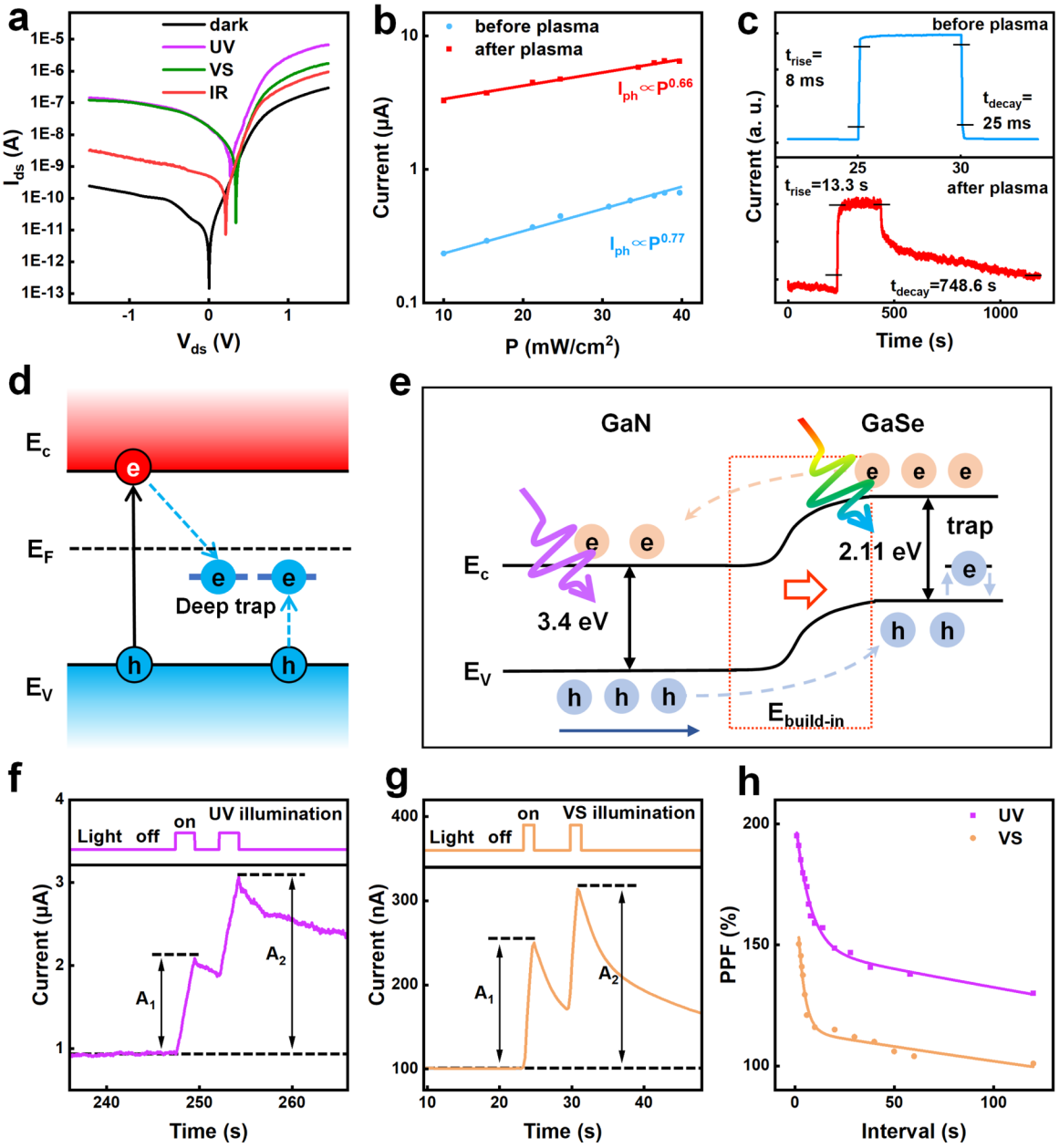

Figure 2. Photoresponse characteristics of optoelectronic devices fabricated on the pristine and Ar-plasma-treated GaSe/GaN heterojunctions. (a) The logarithmic $I-V$ curve of the plasma-treated GaSe/GaN device obtained under IR, VS and UV illumination. (b) Linear fitting of the logarithmic plot of photocurrent (at the V_{ds} of 1.5 V) to the incident power intensity according to the function $I_{ph} = AP^{\theta}$. (c) Single pulse of the $I-t$ curve under shutter-controlled VS illumination showing the typical photoresponse time. (d) Schematic energy band diagram of the Ar-plasma-treated GaSe film with deep trap levels as trapping centers of photoexcited carriers. (e) Schematic energy band diagram illustrating the photoresponse mechanism of UV and VS illumination on the GaSe/GaN heterojunction. (f,g) PPF behavior triggered by two consecutive pulses of UV and VS illumination, respectively. (h) PPF index as a function of the spike time interval.

the A^1_{1g}, E^1_{2g}, and A^2_{1g} vibration modes of GaSe in the pure 2H phase.[32−34] The Raman peak of Ga_2O_3 is not observed. In order to further investigate the effect of Ar-plasma on the electron band structure of the GaSe film, PL characterization under 532 nm laser excitation was conducted, as displayed in Figure 1h. The prominent peak at 578 nm obtained on both samples confirms that the band gap is mostly preserved after the Ar-plasma treatment. Interestingly, the peak intensity even increases a bit, although the full width at half-maximum (fwhm) increases as well. These features are attributed to the presence of in-gap defect states, which could enhance the radiative recombination rate.[35] It has been reported that structural defects could facilitate radiative recombination of direct free excitons.[36] The fwhm increase is not surprising, since slight lattice disorder has been induced by the defects. This evaluation could further confirm that our MArP treatment on GaSe has successfully promoted charge trapping centers without causing unwanted damage.

2.2. Prolonged Photoresponse Time of the Ar-Plasma-Treated Devices. The photoresponse characteristics of the devices fabricated on pristine GaSe/GaN and Ar-plasma-treated GaSe/GaN have been investigated under the illumination of varying wavelengths from a high-pressure Xe lamp equipped with bandpass filters. Plasma-treated GaSe/

https://doi.org/10.1021/acsami.4c22477
ACS Appl. Mater. Interfaces 2025, 17, 14257−14268

GaN devices show superior photoelectric performance and broad-band character, as shown in Figure 2a. The pristine and plasma-treated devices' photoresponse to the UV, VS, and near IR illumination is shown in the complete data sets in Figures S3 and S4. A comparison of the two data sets could reveal that the photocurrent increased dramatically on the Ar-plasma treated sample. It implies Ar-plasma treatment is helpful for enhancing the photoresponsivity by creating defect-related midgap states that trap carriers and give rise to a helpful gating effect.[37] As shown in Figure S5, under UV and VS illumination, the maximum photoresponsivity is 1.1 A/W and 0.78 A/W, while the best detectivity values are 2.3×10^{11} Jones and 5.1×10^{10} Jones, respectively. The result shows that the epitaxially grown GaSe/GaN heterostructure device has a desirable photoresponse performance comparable with other GaSe-based optoelectronic devices.[34,38,39] Such a high performance can be attributed to the clean interface in the GaSe/GaN heterojunction grown under UHV conditions and the avoidance of structural damage after plasma treatment. In Figure 2b, the photocurrent curves obtained at a 1.5 V bias as a function of the incident light intensity are plotted and fitted with this relation $I_{ph} = AP^{\theta}$. I_{ph} is the measured photocurrent ($I_{ph} = I_{light} - I_{dark}$), and A is a constant. The index θ is the fitted parameter related to the trapping and recombination processes of the photocarriers.[40] The deviation of θ from 1 indicates the contribution of trapping levels. Our result shows that θ dropped from 0.77 to 0.66 due to the plasma treatment, which confirmed that the Ar-plasma treatment indeed influenced the trapping and recombination process by providing more defect states.

Additionally, the photoresponse time was significantly prolonged after the Ar-plasma treatment. Specifically, the rising (decaying) time under VS illumination has been prolonged from ∼8 ms (∼25 ms) to ∼13.3 s (748.6 s), as shown in Figure 2c. The UV photoresponse time has also been prolonged (Figure S6). Statistical results reveal that the Ar-plasma treatment-induced photoresponse decay time prolongation ratio is about 10^4. Similarly, Rehman et al. reported that 8 s of oxygen plasma treatment-induced defects in GaSe could prolong the decay time from 20 to 665 s.[24] This phenomenon can be attributed to the trapping effect of defect-related in-gap levels, since the decay time τ_{decay} is composed of the intrinsic carrier lifetime τ_r and trapping level occupation time τ_t before recombination. The latter is determined by the energy difference between the trap states and the valence band edge ΔE as $\tau_t \propto \exp\left(\frac{\Delta E}{kT}\right)$, which is a simple quantum thermodynamic process. Therefore, the deep levels with large ΔE could cause huge latency in the recombination, as displayed in the schematic band diagram in Figure 2d. On the other hand, the shallow trap levels would reduce the decay time by promoting the recombination, as shown in Figure S7. Early works also confirm that point-like native defects like Se vacancies in GaSe will cause deep traps.[41,42] Eventually, we can arrive at the scenario depicting the excitonic dynamics in our device under broadband light illumination, as shown in the schematic band diagram in Figure 2e. The VS and UV illumination generate photoexcited carriers in the GaSe and GaN side of the heterojunction, respectively. Then, the carriers are spontaneously separated by the built-in field, contributing to photocurrent with significant delay due to the deep trapping centers.

To further verify the effect of mild Ar-plasma treatment, we carried out oxygen-plasma and excessive Ar-plasma treatment of the GaSe film as control experiments. As shown in Figure S8, our optimized oxygen-plasma treatment gives weaker prolongation of the decay time compared with that of Ar-plasma treatment. It can be attributed to the lack of Se vacancy-induced midgap levels since oxygen-plasma would give rise to stable oxide clusters with stable chemical bonds rather than Se vacancies.[43,44] Meanwhile, the surface plasma treatment would give rise to an inhomogeneous distribution of defects perpendicular to the surface, as revealed by the TEM images in Figure S9. The defect penetration depth would be tuned by the plasma dosage, which would significantly influence the decay time of the device, as shown in Figure S10. Eventually, the excessive Ar-plasma with enhanced RF power or longer exposure time gives a short decay time due to the collapse of the band gap caused by the damage of the crystalline structure. Therefore, our optimized in situ mild Ar-plasma treatment is superior to the traditional plasma treatment in the aspects of maintaining the structural order while introducing the appropriate density of defects required as charge trapping centers.

Based on the prolonged decay time, we moved one step further in the investigation of the paired pulse facilitation (PPF) performance of Ar-plasma treated devices. The PPF is a benchmark synaptic behavior that refers to the enhancement of the postsynaptic response for the second pulse facilitated by the first one when the pair of pulses is applied in rapid succession.[45,46] As demonstrated in Figure 2f,g, when the pair of UV and VS optical pulses (pulse width:1 s; interval: 1 s) is applied to the device, the amplitude of the photocurrent of the second pulse (A_2) is much higher than that of the first one (A_1). This behavior can be estimated by the PPF index defined $\mathrm{PPF} = \frac{A_2}{A_1} \times 100\%$, which follows the double-exponential function:

$$\text{PPF index} = 1 + C_1 \times \exp\left(-\frac{\Delta t}{\tau_1}\right) + C_2 \times \exp\left(-\frac{\Delta t}{\tau_2}\right) \quad (1)$$

where Δt is the pulse interval; C_1 and C_2 are the initial facilitation magnitudes; τ_1 and τ_2 are the characteristic relaxation times of the rapid and the slow decay term, respectively. The PPF data points acquired at various pulse intervals Δt are fitted into the curves in Figure 2h, revealing that the PPF index can reach 195% (UV) and 150% (VS) while maintaining a high value until Δt increases to ∼10 s, which shows superior performance among other synaptic devices as shown in Table S1. By fitting the data according to function (1), the characteristic relaxation times can be derived as τ_1 = (UV: 6.83 s; VS: 3.36 s) and τ_2 = (UV: 619.05 s; VS: 612.98 s), respectively. The calculated τ_2 is at least about 1 order of magnitude larger than τ_1, showing a resemblance to the decay dynamics observed in biological synapses.[47] These results confirmed that the Ar-plasma-treated GaSe/GaN device could fulfill the requirements of the designed artificial optoelectronic synapse.

2.3. Synaptic Plasticity of Single and Coupled Devices. The synaptic plasticity of the devices was systematically evaluated under the illumination of shutter-controlled VS and UV pulses. Specifically, the EPSC was measured under sequences of consecutive optical pulses with varying numbers, frequencies, or power intensities to investigate the SNDP,

https://doi.org/10.1021/acsami.4c22477
ACS Appl. Mater. Interfaces 2025, 17, 14257−14268

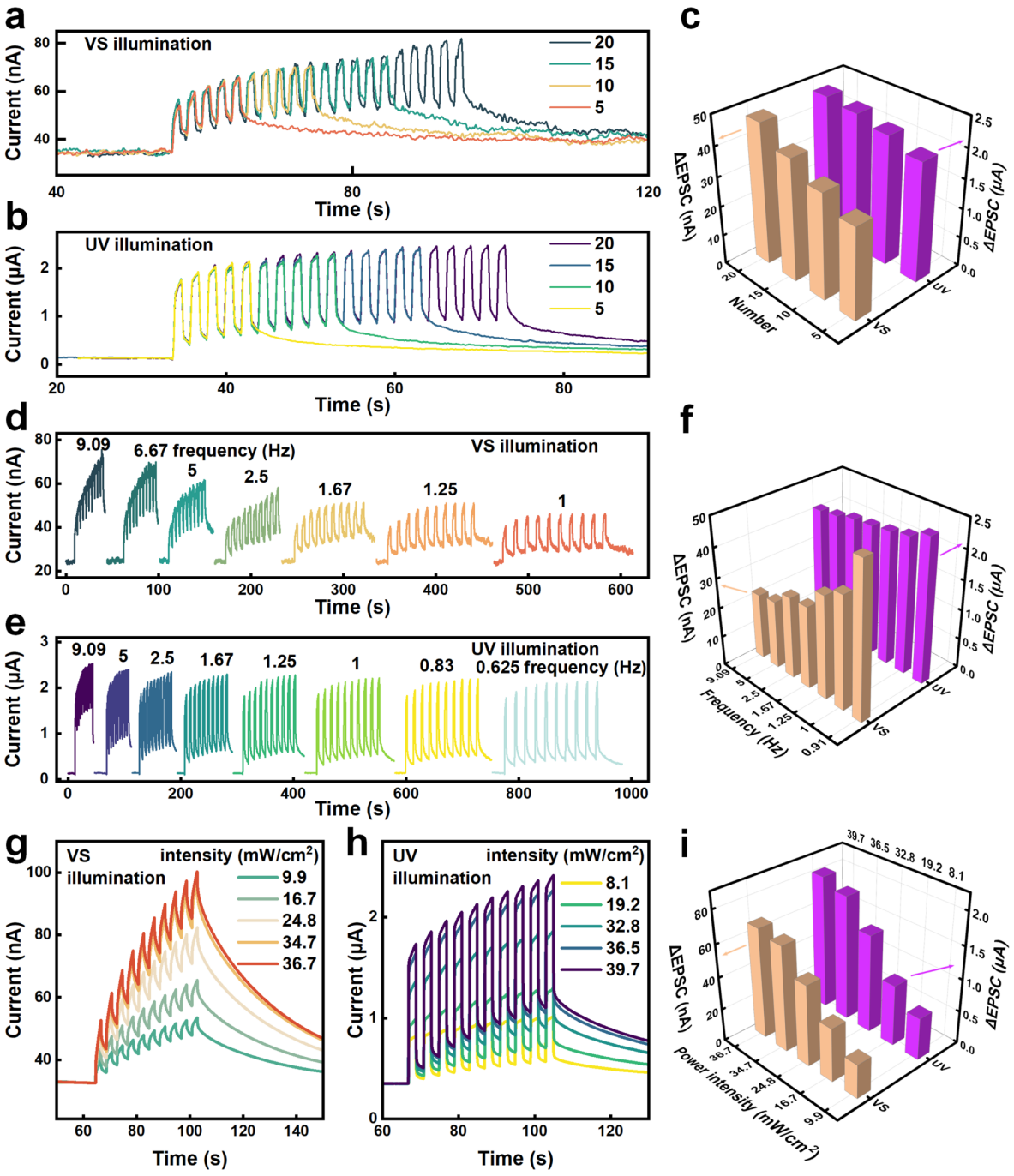

Figure 3. (a–c) Spike-number-dependent plasticity of the devices. (a,b) EPSC triggered by 5, 10, 15, and 20 optical pulses of (a) VS and (b) UV illumination. The pulse duration and intervals are both 1 s. (c) The changes of EPSC (ΔEPSC) depend on the pulse numbers. (d–f) SRDP of the devices. (d,e) EPSC triggered by 10 consecutive optical pulses of (d) VS and (e) UV illumination of varying frequencies. (f) ΔEPSC depends on the pulse frequencies. (g–i) SIDP of the devices. (g,h) EPSC triggered by 10 optical pulses of (g) VS and (h) UV illumination of varying power intensities. (i) ΔEPSC depends on the pulse power intensities.

SRDP, and SIDP, respectively. Figure 3a,b shows the EPSCs produced by a stimulus sequence consisting of 5, 10, 15, and 20 VS (UV) optical pulses. Statistical results in Figure 3c reveal that the changes of EPSC (ΔEPSC) do not show a pronounced decline up to 20 pulses for both VS and UV stimuli, implying a robust SNDP of the devices, which would guarantee a long-time memory capability of the artificial synapses. Following the end of the pulse sequence, an accumulated decay time of the EPSCs can be observed (Figure 3a,b), revealing a forgetting curve of the synapses similar to that of biological nerves. These results imply the learning process of these devices can be effectively enhanced with multiple memorizations.

The learning efficiency also depends on the length of the learning intervals. Figure 3d,e shows the EPSCs produced by ten optical pulses of varying frequencies for VS and UV, respectively. The EPSC shows a trend of decline for a lower frequency of VS stimuli, while the EPSC triggered by UV stimuli remains strong, as shown in Figure 3f. Such SRDP behavior implies that the learning is more efficient for UV

https://doi.org/10.1021/acsami.4c22477
ACS Appl. Mater. Interfaces 2025, 17, 14257−14268

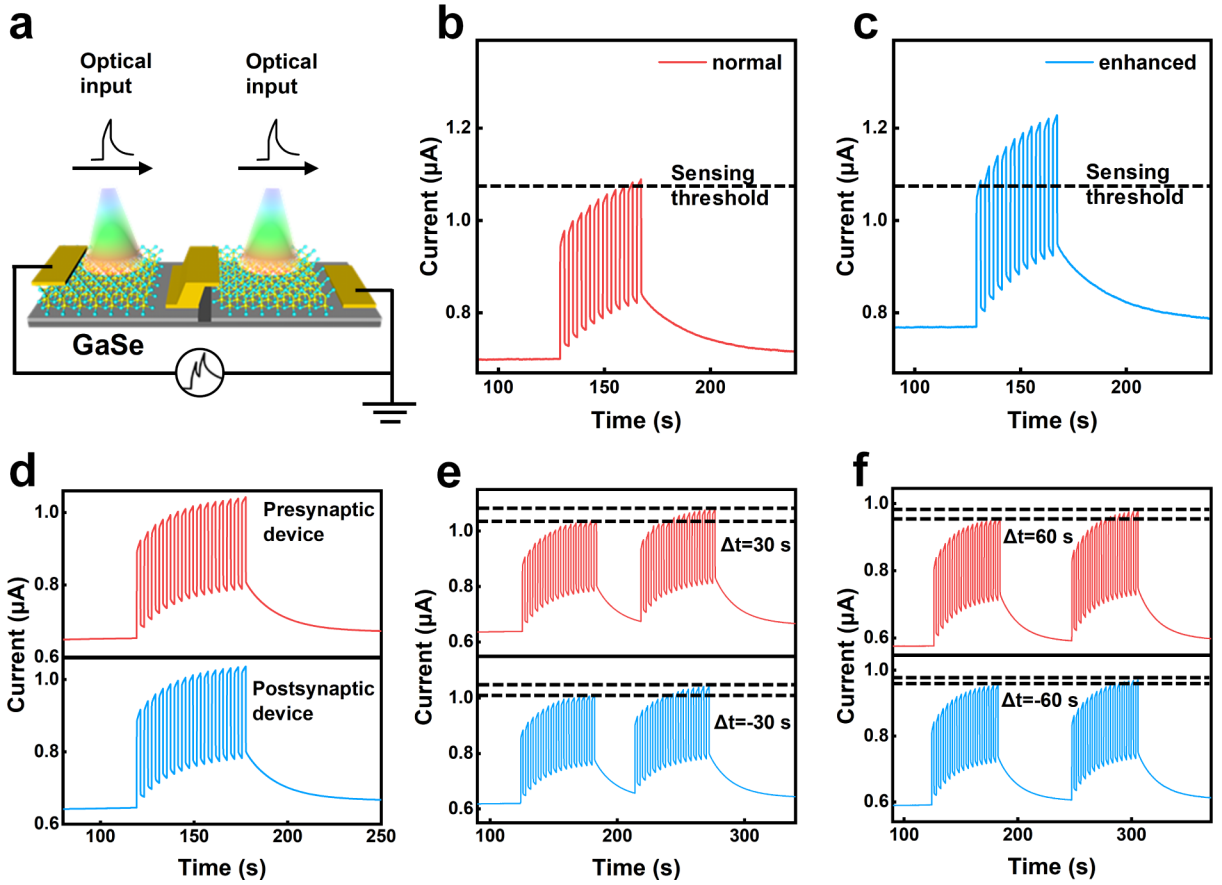

Figure 4. (a) Schematic illustration of two intercoupled GaSe devices linked by the electrode. (b) EPSC triggered when only one synaptic device receives optical pulses. The pulse duration and interval are both 2 s. (c) EPSC triggered when both synaptic devices receive optical pulses, the photocurrent distinctly increases. (d) EPSC of presynaptic and postsynaptic device triggered by optical pulses separately. (e–f) EPSC of multisynapse devices triggered by a pair of spatiotemporally correlated optical pulse sequences.

stimuli, originating from the high UV sensitivity of the heterojunction. Figure 3g,h shows the EPSCs induced by 10 optical pulses with different light intensities, and the EPSCs clearly increase with the increasing light intensity, as shown in Figure 3i. It reveals that intensive stimuli give rise to a steeper forgetting curve, resembling the behavior of biological nerves. The width of single pulses is another factor that influences the forgetting curve in a similar fashion, as displayed in Figure S11. Moreover, the effect of plasma treatment shows great duration as the device maintains excellent synaptic behavior after storing under ambient conditions for two months (Figure S12). To sum up, the modulation of the pulse number, width, frequency, and intensity of incident optical stimuli could effectively influence the EPSCs of the device, giving rise to the excellent synaptic plasticity of artificial synapses based on Ar-plasma treated GaSe/GaN heterojunction.

Additionally, the influence of intercoupling between presynaptic and postsynaptic activities on signal transmission between synapses was investigated. When a single stimulus signal is received by the multisynaptic neuron system, the association between synapses would enhance the sensitivity and memory behavior. The large-scale homogeneous film is very suitable for fabricating the multisynapse device array. To elucidate the interaction between synapses, two individual synaptic devices are intercoupled by sharing a common electrode, as shown in Figure 4a. It shows that the EPSC of the system could be enhanced when both devices receive optical stimuli. As shown in Figure 4b,c, it takes nine single pulses to reach the threshold for one synaptic device to receive the stimulus, while it only takes one pulse when both of the synaptic devices receive optical signals.

In such a multisynapse system, the time intervals of spikes that trigger two synaptic devices significantly influence the presynaptic and postsynaptic activities due to the formation of coupling. Here, two optical stimulus sequences with different intervals are applied on the pre- and postsynaptic devices, respectively. Figure 4d shows the EPSC when presynaptic and postsynaptic devices receive optical stimuli separately. Figure 4e,f shows the EPSC of the intercoupled synaptic devices receiving optical stimulus sequences with positive and negative time intervals, respectively. Under this circumstance, the photocurrent generated by the first spike (A_1) is added on top of that generated by the second spike, consequently increasing the amplitude of the final current (A_2). Therefore, the latter EPSC triggered by the second optical stimulus sequence is always larger than that triggered by the first one, regardless of the relative time intervals. This implies the potentiation of the system for enhancing the synaptic weight between the two synapses. Such enhancement can be calculated by $(A_2-A_1)/A_1$, which decreases with the ascending time intervals between the sequences of stimuli.[48] Therefore, the change of the EPSC is dependent on the time interval between optical stimulus sequences. When the time interval increases, the EPSC will decay, suggesting that the memory of

https://doi.org/10.1021/acsami.4c22477
ACS Appl. Mater. Interfaces 2025, 17, 14257–14268

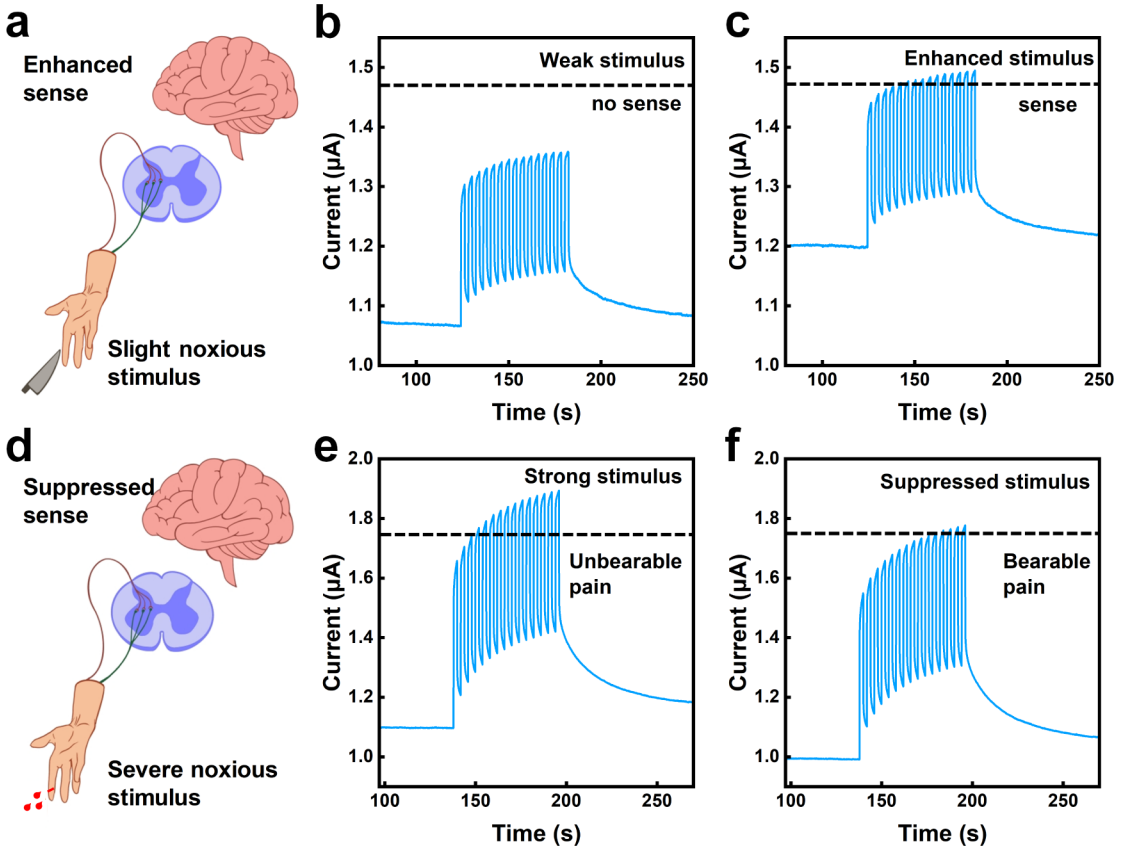

Figure 5. Simulation of the adaptive pain perception. (a–c) Under low stimuli, the nociceptors cannot generate enough potential (a), the current response remains below the sensing threshold level (b), the effect of stimuli can be amplified through the modulation of the bias applied on the device, and then, the photocurrent rises above the threshold level (c). (d–f) Under strong illumination the nociceptors constantly receive powerful stimuli (d), the generated photocurrent quickly rises above the pain threshold level and continuously stays at high levels (e), modulating the bias applied on the device can suppress the effect of stimuli, and photocurrent falls below the threshold level (f).

the events is weakened over time. The neuronal circuit formed by intercoupling multiple biological synapses enables the brain to accomplish complex neurobehaviors such as adapting and learning. Artificial synapses could also benefit from such coupling to acquire the capability of stimulating brain-like behaviors. Thus, future neuromorphic chips based on arrays of intercoupled synapses will be able to satisfy the demand of big data processing for artificial intelligence.

2.4. Simulation of the Adaptive Pain Perception and Associative Learning. The high performance in synaptic plasticity enables the GaSe/GaN-based artificial synapses to simulate neurobehaviors for neuromorphic computing. To demonstrate such capability of our devices, simulations of the classic neurobehaviors, i.e., adaptive pain perception and associative learning, have been investigated.

For pain perception in biological systems, nociceptors are detectors for noxious stimuli and are essential for taking necessary reactions to avoid potential damages. They sense signals of noxious stimuli and compare the amplitude of the signal with the threshold to determine whether an action potential should be generated and sent to the brain or not.[49] Meanwhile, nociceptors also need to modify the intensity of the received signals under certain conditions to prevent the potential excessive damaging inputs while maintaining the body's integrity. As shown in Figure 5, the simulation of the adaptive pain perception has been realized in the GaSe/GaN-based artificial synapses. When the stimuli are not strong enough, the generated photocurrent remains at a low level and cannot reach the sensing threshold. The nociceptors thereby cannot generate action potential to be sent to the brain, and the harmful stimulus will not cause pain perception (Figure 5a,b). However, sensing slight stimuli is necessary for avoiding potential severe injury, for instance, when the finger touches the blade of a rusty knife, as demonstrated in Figure 5a. To solve this problem in the artificial synapses, the response signal strength can adapt by increasing the bias according to the requirement of the threshold level (Figure 5c), corresponding to enhancing the pain perception by improving the nociceptors' sensitivity. On the contrary, when the intensity of stimuli constantly stays at high levels, the response signal quickly exceeds the threshold level, which reflects a situation of unbearable pain sensation due to the perception of pain from a severe injury, as shown in Figure 5d,e. After some time, the human body would adapt the pain sensation to a bearable level until it healed. Similarly, to avoid constant super high response current in the artificial synapses, the reduced bias could be applied to the device to maintain the response signal at a value slightly above the threshold, as shown in Figure 5f. These phenomena demonstrate that the simulation of nociceptors can be realized in our artificial synapses, nicely mimicking the adaptive signal transmission of neural networks under extreme conditions.

Next, the simulation of associative learning in the GaSe/GaN-based artificial synapses was investigated. Making connections through associative learning is a basic function of living organisms. Such an association begins to be

https://doi.org/10.1021/acsami.4c22477
ACS Appl. Mater. Interfaces 2025, 17, 14257–14268

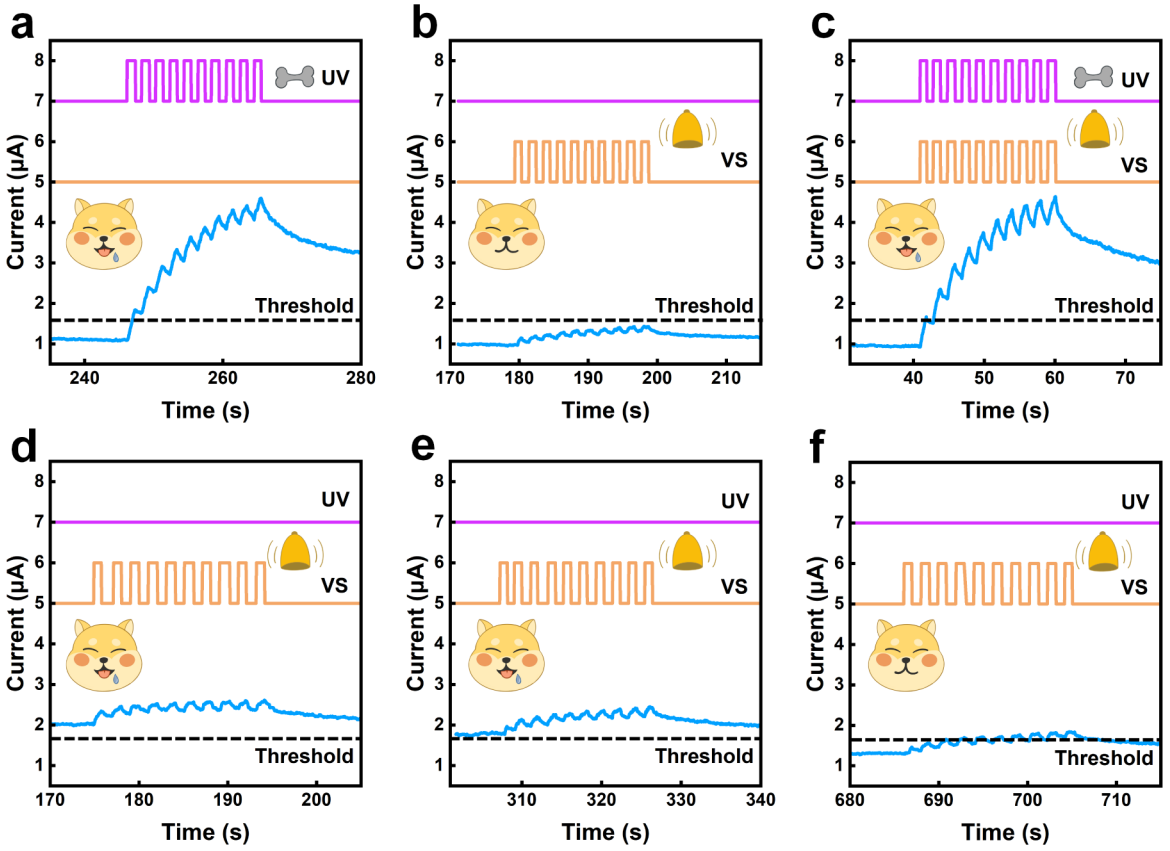

Figure 6. Simulation of the associative learning via classical conditioning Pavlov's dog experiment. (a) Optical pulses with 365 nm (width and interval: 1 s) are introduced as food/unconditioned stimulation and lead to an efficient unconditioned response (salivation). (b) Optical pulses with 640 nm are introduced as bell ringing/conditioned stimulation and do not lead to an efficient conditioned response before training (current < 1.6 μA, no salivation). (c) Training the device to create a strong association and to enhance its memory ability. (d,e) After training conditioned stimuli (optical pulses with 640 nm) alone could trigger salivation. (f) The photocurrent decreased below the salivation threshold when triggered by conditioned stimuli alone without accompanying unconditioned stimuli for about 5 min, indicating extinction of associative memory.

established when two events occur simultaneously. Later on, when one event occurs, the other one is also memorized and recalled.[50] For living organisms, integrating multiple types of signals can enhance their adaptation to different environmental changes. When learning efficiency is improved, it is also essential to eliminate redundant information. The associative learning behavior of the brain in the famous Pavlov's dog experiments has been successfully simulated in our optoelectronic synapse. The broadband character of GaSe/GaN allows the device to perform an all-optical modulation. Here, an input sequence consisting of ten UV optical pulses was used to mimic the food (unconditioned stimuli) activating salivation (unconditioned response) from the postsynaptic terminal. In comparison, another input sequence consisting of ten VS optical pulses was used to mimic the bell (conditioned stimuli) activating a conditioned response for the dog. The dog would salivate when it noticed food, marked by a corresponding high-level current above the salivation response threshold (1.6 μA) as shown in Figure 6a. Before training, due to the lack of associative learning, only a slight increase of photocurrent was achieved without reaching the memory threshold, indicating that the bell ring alone would not lead to any salivation response, as shown in Figure 6b. Figure 6c shows the training routine with food (UV optical pulses) and bell (VS optical pulses) stimuli. At this stage, UV and VS optical pulses were applied simultaneously to the device. Thus, a very high response to trigger salivation was achieved and retained due to the memory property, mimicking the dog's learning to associate the ring (conditioned stimuli) with food (unconditioned stimuli).

As shown in Figure 6d,e, the training routine enhanced the conditioned response, and the subsequent conditioned response alone could produce EPSCs higher than the salivation threshold. This effect could remain for about 5 min without another training routine, and then, the EPSCs decreased below the salivation response threshold, as shown in Figure 6f, indicating that the temporarily established association underwent a decay process over time, resembling memory loss in biological systems. To rebuild the association, another training routine is needed. These phenomena demonstrate that the simulation of complicated synaptic behaviors, like associative learning, can easily be realized in our artificial synapses, which further confirms that our Ar-plasma-treated GaSe/GaN heterojunction could be used as reliable artificial optoelectronic synapses.

3. CONCLUSION

In conclusion, we have reported large-scale epitaxial GaSe/GaN heterojunction-based optoelectronic artificial synapses with broadband perception and tunable memory capability enabled by a tailored mild Ar-plasma treatment. The GaSe/GaN optoelectronic devices show broadband photoresponse in the UV and VS regimes. Our optimized Ar-plasma treatment could effectively tune the synapse functions of the devices by

https://doi.org/10.1021/acsami.4c22477
ACS Appl. Mater. Interfaces 2025, 17, 14257−14268

creating atomic-scale structural defects that provide deep trap states in the band gap, which could significantly prolong the lifetime of photocarriers by a factor of 10^3. This treatment is superior to the traditional oxygen plasma treatment, since it could minimize the structural damage and unwanted contamination to the material. Thus, the devices could be used as artificial optical synapses capable of realizing essential synaptic functions, including PPF, EPSC, SIDP, SNDP, and SRDP. Furthermore, because of the intrinsic electrical tunability and broadband photoresponse characteristics of the devices, the benchmark synaptic behaviors of adaptive pain perception and associative learning can be nicely simulated. This work provides a new strategy to realize robust artificial optoelectronic synapses in the semiconductor technology-compatible 2D/3D hybridized heterostructure, which may find application in artificial neuromorphic computing.

4. EXPERIMENTAL SECTION

4.1. Epitaxial Growth of the GaSe Layer. The n-doped GaN(0001) substrates (4.5 ± 0.5 μm GaN on Sapphire, Si-doped, Suzhou Nanowin Science & Technology CO. LTD) were mounted on holders and transferred into the PVD chamber with a base pressure of 1×10^{-9} mbar. They were then heated to 873 K for 30 min before the deposition of films to remove the gas adsorbed on the surface. High-purity Ga_2Se_3 powders (99.99%, Alfa Aesar) evaporated from a Knudsen cell were deposited onto the GaN substrate, which was kept at 523 ± 10 K. GaSe films were obtained after a growth time of 15−20 min. The samples were subsequently annealed at the growth temperature for 30 min, which mainly enhances the quality of the films.

4.2. Mild Ar-Plasma Treatment. The plasma treatment was accomplished by Ar plasma (PT-5ST, SANHOPTT) for 5 s with a 15 W RF power for surface modulation. The flow rate of Ar was 15 sccm.

4.3. Device Fabrication. The electrodes were patterned in a home-built ultrahigh vacuum chamber with a base pressure of 1×10^{-8} mbar over the heterostructure, and metal layers of Au (~100 nm) were deposited by using a custom-made metal shadow mask with an Au evaporator.

4.4. Material Characterization. The morphology of the prepared GaSe/GaN heterojunction was recorded by a field-emission scanning electron microscope (MIRA3-LMH, Tyco Electronics) at 15 kV. The surface morphologies and thickness of the film were measured by atomic force microscopy (SPM-9700HT). The phase of the GaSe film was confirmed by the characteristic peaks in the Raman spectroscopy, which were obtained from a laser Raman spectrometer equipped with a 532 nm laser (Renishaw InVia Qontor). PL spectroscopy (HORIBA) was performed with a 350 nm excitation line.

4.5. Optoelectronic Transport Measurement. All of the electrical measurements were performed at room temperature (300 K) on a probe station under an ambient atmosphere. The electrical performance was analyzed with a dual-channel source meter (Keithley 2636B). The optical responses were measured at various power densities using a Keithley 2636B with a high-pressure Xe lamp (CME-SL300, Microenerg) equipped with ultraviolet (300−400 nm), visible (400−780 nm), and infrared (800−2500 nm) filters. A light source for the classical conditioning Pavlov's dog experiment is a light-emitting diode (Oaebt OF-20B, λ = 365, 640, and 805 nm), and the input optical sequence is controlled by a signal generator (MHS5200A).

■ ASSOCIATED CONTENT

Supporting Information

The Supporting Information is available free of charge at https://pubs.acs.org/doi/10.1021/acsami.4c22477.

Growth conditions for GaSe films; AFM image and height profile of pristine and plasma-treated GaSe surface; SEM image and EDS spectrum of the GaSe film after MArP treatment; SEM image of GaSe/GaN interface; high-resolution TEM image of the type, depth, and distribution of the defects; the $I-V$ curves of pristine and plasma-treated GaSe film; single pulse of the $I-t$ curve of pristine and plasma-treated GaSe film; photoresponsivity and detectivity of plasma-treated GaSe/GaN device under UV and VS illumination; band structure of GaSe film containing recombination center and shallow trap; influence of oxygen plasma treatment to the photoresponse of GaSe film; the relation between plasma dose and photoresponse time; comparison of the PPF from this work to literatures; spike-duration dependent plasticity of GaSe/GaN devices; ambient condition stability of the devices (PDF)

■ AUTHOR INFORMATION

Corresponding Authors

Hong Lei − *Shaanxi Institute for Pediatric Diseases, Xi'an Children's Hospital, Xi'an 710003, China*; Email: leihongnk@163.com

Yi Pan − *Center for Spintronics and Quantum Systems, State Key Laboratory for Mechanical Behavior of Materials, Xi'an Jiaotong University, Xi'an 710049, China*; orcid.org/0000-0003-1978-475X; Email: yi.pan@xjtu.edu.cn

Authors

Yunan Lin − *Center for Spintronics and Quantum Systems, State Key Laboratory for Mechanical Behavior of Materials, Xi'an Jiaotong University, Xi'an 710049, China*

Xuecen Miao − *Center for Spintronics and Quantum Systems, State Key Laboratory for Mechanical Behavior of Materials, Xi'an Jiaotong University, Xi'an 710049, China*

Yinuo Zhang − *Center for Spintronics and Quantum Systems, State Key Laboratory for Mechanical Behavior of Materials, Xi'an Jiaotong University, Xi'an 710049, China*

Lan Li − *Center for Spintronics and Quantum Systems, State Key Laboratory for Mechanical Behavior of Materials, Xi'an Jiaotong University, Xi'an 710049, China*

Jiaqi Yang − *Center for Spintronics and Quantum Systems, State Key Laboratory for Mechanical Behavior of Materials, Xi'an Jiaotong University, Xi'an 710049, China*

Complete contact information is available at: https://pubs.acs.org/10.1021/acsami.4c22477

Author Contributions

Y.P. and H.L. conceived and supervised the experiments. Y.L. synthesized samples, fabricated the devices, and performed the measurements with the help of X.M., Y.Z., L.L., and J.Y. Y.L., H.L., and Y.P. wrote the manuscript with the input of all authors.

Notes

The authors declare no competing financial interest.

https://doi.org/10.1021/acsami.4c22477
ACS Appl. Mater. Interfaces 2025, 17, 14257−14268

■ ACKNOWLEDGMENTS

This work was financially supported by the National Key Research and Development Program of China (grant no. 2022YFA1204100) and the National Natural Science Foundation of China (grant nos. 82200728 and 12074302). We thank the Instrument Analysis Center of Xi'an Jiaotong University for their assistance with TEM, Raman, SEM, and AFM measurements.

■ REFERENCES

(1) Merolla, P. A.; Arthur, J. V.; Alvarez-Icaza, R.; Cassidy, A. S.; Sawada, J.; Akopyan, F.; Jackson, B. L.; Imam, N.; Guo, C.; Nakamura, Y. A million spiking-neuron integrated circuit with a scalable communication network and interface. *Science* **2014**, *345* (6197), 668−673.

(2) Prezioso, M.; Merrikh-Bayat, F.; Hoskins, B. D.; Adam, G. C.; Likharev, K. K.; Strukov, D. B. Training and operation of an integrated neuromorphic network based on metal-oxide memristors. *Nature* **2015**, *521* (7550), 61−64.

(3) Zidan, M. A.; Strachan, J. P.; Lu, W. D. The future of electronics based on memristive systems. *Nat. Electron.* **2018**, *1* (1), 22−29.

(4) Zador, A.; Escola, S.; Richards, B.; Olveczky, B.; Bengio, Y.; Boahen, K.; Botvinick, M.; Chklovskii, D.; Churchland, A.; Clopath, C. Catalyzing next-generation Artificial Intelligence through NeuroAI. *Nat. Commun.* **2023**, *14* (1), 1597.

(5) Liu, C.; Yan, X.; Song, X.; Ding, S.; Zhang, D. W.; Zhou, P. A semi-floating gate memory based on van der Waals heterostructures for quasi-non-volatile applications. *Nat. Nanotechnol.* **2018**, *13* (5), 404−410.

(6) Manipatruni, S.; Nikonov, D. E.; Young, I. A. Beyond CMOS computing with spin and polarization. *Nat. Phys.* **2018**, *14* (4), 338−343.

(7) Kuzum, D.; Yu, S.; Wong, H.-S. P. Synaptic electronics: Materials, devices and applications. *Nanotechnology* **2013**, *24* (38), 382001.

(8) Sudhof, T. C. The cell biology of synapse formation. *J. Cell Biol.* **2021**, *220* (7), No. e202103052.

(9) Sun, W.; Gao, B.; Chi, M.; Xia, Q.; Yang, J. J.; Qian, H.; Wu, H. Understanding memristive switching via in situ characterization and device modeling. *Nat. Commun.* **2019**, *10* (1), 3453.

(10) Connor, S. A.; Siddiqui, T. J. Synapse organizers as molecular codes for synaptic plasticity. *Trends Neurosci.* **2023**, *46* (11), 971−985.

(11) Wang, Y.; Yin, L.; Huang, W.; Li, Y.; Huang, S.; Zhu, Y.; Yang, D.; Pi, X. Optoelectronic Synaptic Devices for Neuromorphic Computing. *Adv. Intell. Syst.* **2021**, *3* (1), 2000099.

(12) Zhao, H.; Dong, Z.; Tian, H.; DiMarzi, D.; Han, M. G.; Zhang, L.; Yan, X.; Liu, F.; Shen, L.; Han, S.-J.; et al. Atomically Thin Femtojoule Memristive Device. *Adv. Mater.* **2017**, *29* (47), 1703232.

(13) Sahu, M. C.; Sahoo, S.; Mallik, S. K.; Jena, A. K.; Sahoo, S. Multifunctional 2D MoS_2 Optoelectronic Artificial Synapse with Integrated Arithmetic and Reconfigurable Logic Operations for In-Memory Neuromorphic Computing Applications. *Adv. Mater. Technol.* **2023**, *8* (2), 2201125.

(14) Chen, K.; Hu, H.; Song, I.; Gobeze, H. B.; Lee, W.-J.; Abtahi, A.; Schanze, K. S.; Mei, J. Organic optoelectronic synapse based on photon-modulated electrochemical doping. *Nat. Photonics* **2023**, *17* (7), 629−637.

(15) Han, S.; Ma, T.; Li, H.; Wu, J.; Liu, R.; Cao, R.; Li, F.; Li, H.; Chen, C. Photoferroelectric Perovskite Synapses for Neuromorphic Computing. *Adv. Funct. Mater.* **2024**, *34* (3), 2309910.

(16) Chen, S.; Lou, Z.; Chen, D.; Shen, G. An Artificial Flexible Visual Memory System Based on an UV-Motivated Memristor. *Adv. Mater.* **2018**, *30* (7), 1705400.

(17) Chen, H.; Wan, T.; Zhou, Y.; Yan, J.; Chen, C.; Xu, Z.; Zhang, S.; Zhu, Y.; Yu, H.; Chai, Y. Highly Nonlinear Memory Selectors with Ultrathin $MoS_2/WSe_2/MoS_2$ Heterojunction. *Adv. Funct. Mater.* **2024**, *34* (15), 2304242.

(18) Zhu, X.; Li, D.; Liang, X.; Lu, W. D. Ionic modulation and ionic coupling effects in MoS_2 devices for neuromorphic computing. *Nat. Mater.* **2019**, *18* (2), 141−148.

(19) Yuan, S.; Qiu, B.; Amina, K.; Li, L.; Zhai, P.; Su, Y.; Xue, T.; Jiang, T.; Ding, L.; Wei, G. Robust and Low-Power-Consumption Black Phosphorus-Graphene Artificial Synaptic Devices. *ACS Appl. Mater. Interfaces* **2022**, *14* (18), 21242−21252.

(20) Park, H. L.; Lee, Y.; Kim, N.; Seo, D. G.; Go, G. T.; Lee, T. W. Flexible Neuromorphic Electronics for Computing, Soft Robotics, and Neuroprosthetics. *Adv. Mater.* **2020**, *32* (15), No. e1903558.

(21) Vasilopoulou, M.; Mohd Yusoff, A. R. B.; Chai, Y.; Kourtis, M.-A.; Matsushima, T.; Gasparini, N.; Du, R.; Gao, F.; Nazeeruddin, M. K.; Anthopoulos, T. D. Neuromorphic computing based on halide perovskites. *Nat. Electron.* **2023**, *6* (12), 949−962.

(22) Jiang, J.; Ling, C.; Xu, T.; Wang, W.; Niu, X.; Zafar, A.; Yan, Z.; Wang, X.; You, Y.; Sun, L. Defect Engineering for Modulating the Trap States in 2D Photoconductors. *Adv. Mater.* **2018**, *30* (40), 1804332.

(23) Constantinou, I.; Lai, T. H.; Hsu, H. Y.; Cheung, S. H.; Klump, E. D.; Schanze, K. S.; So, S. K.; So, F. Effect of Thermal Annealing on Charge Transfer States and Charge Trapping in PCDTBT: PC70BM Solar Cells. *Adv. Electron. Mater.* **2015**, *1* (9), 1500167.

(24) Rehman, S.; Khan, M. A.; Kim, H.; Patil, H.; Aziz, J.; Kadam, K. D.; Rehman, M. A.; Rabeel, M.; Hao, A.; Khan, K. Optically Reconfigurable Complementary Logic Gates Enabled by Bipolar Photoresponse in Gallium Selenide Memtransistor. *Adv. Sci.* **2023**, *10* (17), 2205383.

(25) Kim, J. J.; Ha, J. M.; Lee, H. M.; Raza, H. S.; Park, J. W.; Cho, S. O. Effect of Electron-Beam Irradiation on Organic Semiconductor and Its Application for Transistor-Based Dosimeters. *ACS Appl. Mater. Interfaces* **2016**, *8* (30), 19192−19196.

(26) Jung, J. H.; Choi, W. Unusual n-type doping of monolayer WSe_2 by CF_4 plasma treatment. *Mater. Lett.* **2021**, *295*, 129865.

(27) Kim, M. S.; Nam, G.; Park, S.; Kim, H.; Han, G. H.; Lee, J.; Dhakal, K. P.; Leem, J.-Y.; Lee, Y. H.; Kim, J. Photoluminescence wavelength variation of monolayer MoS_2 by oxygen plasma treatment. *Thin Solid Films* **2015**, *590*, 318−323.

(28) Han, Z.; Murdock, A. T.; Seo, D.; Bendavid, A. Recent progress in plasma-assisted synthesis and modification of 2D materials. *2D Mater.* **2018**, *5* (3), 032002.

(29) Ji, X.; Paulsen, B. D.; Chik, G. K. K.; Wu, R.; Yin, Y.; Chan, P. K. L.; Rivnay, J. Mimicking associative learning using an ion-trapping non-volatile synaptic organic electrochemical transistor. *Nat. Commun.* **2021**, *12* (1), 2480.

(30) Li, X.; Luo, S.; Xue, F. Effects of synaptic integration on the dynamics and computational performance of spiking neural network. *Cogn. Neurodyn.* **2020**, *14* (3), 347−357.

(31) Li, H.; Tsai, C.; Koh, A. L.; Cai, L.; Contryman, A. W.; Fragapane, A. H.; Zhao, J.; Han, H. S.; Manoharan, H. C.; Abild-Pedersen, F. Correction: Corrigendum: Activating and optimizing MoS_2 basal planes for hydrogen evolution through the formation of strained sulphur vacancies. *Nat. Mater.* **2016**, *15* (3), 364−364.

(32) Ben Aziza, Z.; Henck, H.; Pierucci, D.; Silly, M. G.; Lhuillier, E.; Patriarche, G.; Sirotti, F.; Eddrief, M.; Ouerghi, A. van der Waals Epitaxy of GaSe/Graphene Heterostructure: Electronic and Interfacial Properties. *ACS Nano* **2016**, *10* (10), 9679−9686.

(33) Diep, N. Q.; Tran, Q. T.; Huynh, T. B. T.; Wen, H. C.; Chou, W. C.; Huynh, S. H.; Le, V. Q.; Chu, Y. H.; Vu, T. T. Growth Mode Transition in Two-Dimensional GaSe on Three-Dimensional GaN/Sapphire Platform: Implication for Self-Powered Photodetection. *ACS Appl. Nano Mater.* **2024**, *7* (3), 3042−3049.

(34) Hu, P.; Wen, Z.; Wang, L.; Tan, P.; Xiao, K. Synthesis of Few-Layer GaSe Nanosheets for High Performance Photodetectors. *ACS Nano* **2012**, *6* (7), 5988−5994.

(35) Manfredotti, C.; Murri, R.; Rizzo, A.; Galassini, S.; Ruggiero, L. Deep hole traps inp-type GaSe single crystals. *Phys. Rev. B* **1974**, *10* (8), 3387−3393.

(36) Cai, H.; Rasmita, A.; Tan, Q.; Lai, J. M.; He, R.; Cai, X.; Zhao, Y.; Chen, D.; Wang, N.; Mu, Z. Interlayer donor-acceptor pair

excitons in $MoSe_2/WSe_2$ moire heterobilayer. *Nat. Commun.* **2023**, *14* (1), 5766.
(37) Tsai, T. H.; Liang, Z. Y.; Lin, Y. C.; Wang, C. C.; Lin, K. I.; Suenaga, K.; Chiu, P. W. Photogating WS_2 Photodetectors Using Embedded WSe_2 Charge Puddles. *ACS Nano* **2020**, *14* (4), 4559−4566.
(38) Ko, P. J.; Abderrahmane, A.; Takamura, T.; Kim, N. H.; Sandhu, A. Thickness dependence on the optoelectronic properties of multilayered GaSe based photodetector. *Nanotechnology* **2016**, *27* (32), 325202.
(39) Demirtas, T.; Odaci, C.; Aydemir, U. Enhanced photoresponse of PVP: GaSe nanocomposite thin film based photodetectors. *Nanotechnology* **2022**, *33* (20), 205506.
(40) Kind, H.; Yan, H.; Messer, B.; Law, M.; Yang, P. Nanowire Ultraviolet Photodetectors and Optical Switches. *Adv. Mater.* **2002**, *14* (2), 158−160.
(41) Rák, Z.; Mahanti, S. D.; Mandal, K. C.; Fernelius, N. C. Defect-induced rigidity enhancement in layered semiconductors. *Solid State Commun.* **2010**, *150* (27), 1200−1203.
(42) Parlak, M.; Qasrawi, A. F.; Erçelebi, Ç. Growth, electrical and structural characterization of β-GaSe thin films. *J. Mater. Sci.* **2003**, *38* (7), 1507−1511.
(43) Li, J.; Bai, J.; Meng, M.; Hu, C.; Yuan, H.; Zhang, Y.; Sun, L. Improved Temporal Response of MoS_2 Photodetectors by Mild Oxygen Plasma Treatment. *Nanomaterials* **2022**, *12* (8), 1365.
(44) Yu, J.; Suleiman, A. A.; Zheng, Z.; Zhou, X.; Zhai, T. Giant-Enhanced SnS_2 Photodetectors with Broadband Response through Oxygen Plasma Treatment. *Adv. Funct. Mater.* **2020**, *30* (24), 2001650.
(45) Wang, X.; Zong, Y.; Liu, D.; Yang, J.; Wei, Z. Advanced Optoelectronic Devices for Neuromorphic Analog Based on Low-Dimensional Semiconductors. *Adv. Funct. Mater.* **2023**, *33* (15), 2213894.
(46) Das, B.; Baek, S.; Niu, J.; Jang, C.; Lee, Y.; Lee, S. Artificial Visual Systems Fabricated with Ferroelectric van der Waals Heterostructure for In-Memory Computing Applications. *ACS Nano* **2023**, *17* (21), 21297−21306.
(47) Jackman, S. L.; Regehr, W. G. The Mechanisms and Functions of Synaptic Facilitation. *Neuron* **2017**, *94* (3), 447−464.
(48) Zhao, S.; Ni, Z.; Tan, H.; Wang, Y.; Jin, H.; Nie, T.; Xu, M.; Pi, X.; Yang, D. Electroluminescent synaptic devices with logic functions. *Nano Energy* **2018**, *54*, 383−389.
(49) Shan, L.; Chen, Q.; Yu, R.; Gao, C.; Liu, L.; Guo, T.; Chen, H. A sensory memory processing system with multi-wavelength synaptic-polychromatic light emission for multi-modal information recognition. *Nat. Commun.* **2023**, *14* (1), 2648.
(50) Li, Q.; Wang, T.; Fang, Y.; Hu, X.; Tang, C.; Wu, X.; Zhu, H.; Ji, L.; Sun, Q.-Q.; Zhang, D. W. Ultralow Power Wearable Organic Ferroelectric Device for Optoelectronic Neuromorphic Computing. *Nano Lett.* **2022**, *22* (15), 6435−6443.

https://doi.org/10.1021/acsami.4c22477
ACS Appl. Mater. Interfaces 2025, 17, 14257−14268